MATERIALS CHEMISTRY
FRONTIERS

RESEARCH ARTICLE

View Article Online
View Journal

Cite this: DOI: 10.1039/d6qm00006a

Self-powered sucrose detection using a superhydrophobic liquid–solid triboelectric nanogenerator

Premkumar Sharad Bhosale,[a] Sugato Hajra,*[a] Swati Panda,[b] Kushal Ruthvik Kaja,[a] Mohamed Belal,[a] Soon Moon Jeong[cd] and Hoe Joon Kim*[a]

Received 5th January 2026,
Accepted 24th February 2026

DOI: 10.1039/d6qm00006a

rsc.li/frontiers-materials

Real-time monitoring of sucrose concentration is essential in intelligent industrial processing, food quality control, and biochemical manufacturing, creating demand for sustainable and autonomous sensing technologies. In this work, a liquid–solid triboelectric nanogenerator (LS-TENG) is developed for simultaneous energy harvesting and sucrose concentration sensing using deionized water (DI) and sucrose solutions as the active liquid medium. The device employs a hydrophobic polytetrafluoroethylene (PTFE) surface as the solid triboelectric layer, enabling repeated charge generation during droplet contact–separation events. Changes in sucrose concentration significantly affect charge density and electrical output, enabling quantitative sensing without external power sources. The developed LS-TENG achieves a maximum output voltage of −37 V and a current of 52 nA, demonstrating efficient conversion of droplet kinetic energy into electrical signals. The sensing mechanism is attributed to sucrose-induced disruption of the hydrogen-bonding network of water, forming sucrose–water interactions that alter solution conductivity and flow behavior. This study introduces a sustainable, self-powered triboelectric sensing probe, offering a promising platform for real-time sucrose monitoring in smart industrial and process-control applications.

1. Introduction

A common substance, sucrose, plays essential roles in consumer goods, biomedicine, and food processing.[1,2] Electro-wettability, electrochemical efficiency, and colloidal stability are essential parameters that significantly affect mass transfer and reaction kinetics in solution systems, as their interactions with solid surfaces strongly influence these processes.[3,4] However, due to the influence of variables such as ionic concentration, pH, and hydrogen bonding, comprehending liquid–solid contact electrification remains challenging.[5,6] By disrupting the natural water–water hydrogen bonds and promoting ion transport, sucrose molecules form intricate multi-hydrogen-bond networks with water, which can significantly affect charge-transfer behavior at surfaces.[7] Despite advances, the fundamental processes governing contact electrification in sucrose-based sensing systems remain unclear, and developing triboelectric sensing platforms to understand and exploit these effects remains challenging.

Triboelectric nanogenerators (TENGs) have become a promising mechanical energy harvesting technology due to their low fabrication costs, lightweight structure, compact form, and high stability.[8–12] They have been employed in various applications, such as robotics, sensing, biomedical applications, and data processing.[13–15] They work especially well for producing electrical output from irregular, low-frequency, low-intensity mechanical motions.[16–19] LS-TENGs offer an appealing way to efficiently employ droplet kinetic energy into useful electrical output for rapid sensing devices.[20,21] Recent investigations have highlighted that the performance of LS-TENG is highly dependent on multiple interacting factors, particularly the choice of surface material.[22] Jiang *et al.* have comprehensively summarized the principles, structures, performance factors, applications, and future challenges of fluid-based TENGs for energy harvesting and self-powered sensing.[23] Kulandaivel *et al.* highlighted ferrofluid–solid TENGs as an advanced solution for harvesting ultra-low-frequency mechanical energy while enabling hybrid energy harvesting.[24] Kulandaivel *et al.* systematically reviewed how surface wettability and hydrophobicity influence contact electrification mechanisms and output performance in LS-TENGs, outlining challenges and future directions for performance optimization.[25] Both artificial and

[a] Department of Robotics and Mechatronics Engineering, Daegu Gyeongbuk Institute of Science and Technology, Daegu 42988, Republic of Korea.
E-mail: joonkim@dgist.ac.kr, sugatohajra@dgist.ac.kr
[b] Department of Electrical Engineering and Computer Science, Daegu Gyeongbuk Institute of Science & Technology (DGIST), Daegu, 42988, Republic of Korea
[c] Department of Advanced Technology, Daegu Gyeongbuk Institute of Science & Technology (DGIST), Daegu 42988, Republic of Korea
[d] Department of Interdisciplinary Engineering, Daegu Gyeongbuk Institute of Science & Technology (DGIST), Daegu 42988, Republic of Korea

naturally derived surfaces, including PTFE, silicon, paper, aloe leaf, and cicada wing, have been explored to understand their influence on charge generation.[26] Beyond chemical structure and intrinsic surface properties, the micro- and nanoscale texture of these materials plays a decisive role in determining wettability, liquid spreading, and contact–separation dynamics, thereby affecting the overall electrical response.[27–29] Simultaneously, liquid characteristics such as ionic strength, pH, and ion mobility regulate charge accumulation and interfacial transfer.[28,30] Environmental parameters such as temperature and humidity further modulate these effects, altering output stability.[31] Moreover, the device's geometric design and electrode configuration are key to optimising performance, also leading to charge-transfer efficiencies.[32,33] Collectively, these insights reveal the broad adaptability of LS-TENG systems across diverse energy harvesting and sensing interfaces, extending to liquid–liquid and gas–liquid domains.[34,35]

Improving the energy conversion efficiency of LS-TENG requires a deep comprehension of how droplet motion affects their electrical response. LS-TENG, configured with only a bottom electrode, relies solely on electrostatic induction, leading to comparatively weaker electrical performance. However, in the case of the double-electrode LS-TENG design, charges build up when a droplet strikes the surface through two mechanisms: the electric double layer (EDL) and electrostatic induction. This process drives electrons to move from the lower electrode (or from the ground in the top-electrode design) toward the upper electrode. A potential difference that generates a measurable electrical output when the droplet spreads across the upper electrode already bearing surface charges. Electrical equilibrium is restored when the induced charges return to their original side as the droplet rolls off and retracts.

Here, the double-electrode configuration-based LS-TENG was systematically evaluated to clarify variations in its performance under different conditions, including substrate angle, droplet height, and pH. Voltage, current, and power were the electrical outputs recorded. A camera captured the visualised droplet motion through the dielectric. The double-electrode arrangement was further shown for two real-world applications with optimal parameters: energy harvesting and real-time detection of sucrose in DI water. This study clarifies the behavior of liquid–solid electrification by demonstrating that sucrose solutions generate an electrical charge upon contact with solid surfaces. Sucrose sensing has been widely explored using enzymatic, electrochemical, optical, and nanomaterial-based approaches. The proposed LS-TENG enables simultaneous energy harvesting and real-time concentration monitoring, in contrast to traditional sucrose-sensing techniques that require external power sources and sophisticated apparatus. LS-TENG enhances sensing sensitivity and charge-generation efficiency by introducing a superhydrophobic surface. This self-powered sensor platform provides strong industrial relevance, such as affordable monitoring in food processing, biochemical production, and smart manufacturing settings. Table S1 shows a comparison of various parameters of traditional sucrose-sensing techniques with the proposed LS-TENG system. By immediately translating liquid–solid contact electrification into detectable electrical signals, a triboelectric solid–liquid probe enables self-powered, real-time sucrose sensing without the need for complex electronics, enzymes, or other power sources. LS-TENG-based sucrose detection offers simplicity, affordability, high robustness in aqueous environments, and ease of integration for *in situ* monitoring, distinguishing it from traditional electrochemical or optical techniques. This study lays the groundwork for the development of improved designs for future LS-TENGs, which will be more efficient, durable, and environmentally adaptable.

2. Experimental details and characterization techniques

For the fabrication of the double-electrode mode LS-TENG device, the acrylic substrate, aluminium electrode, and PTFE solid layer were first prepared. The aluminum (Al) electrode was purchased from 3M, USA. The acrylic sheet used as the substrate was purchased from Daiso, Korea. PTFE film was procured from Alibaba, China, and sucrose powder was obtained from Alfa Aesar, USA, and used without purification. The dielectric layer was made of a 3×6 cm^2 PTFE sheet bearing a thickness of 0.01 cm. After 20 minutes of ultrasonic cleaning in ethanol and deionised water, the sheet was dried for 12 hours at 70 °C in an oven. The supporting substrate was made to be 5×6 cm^2 and 0.3 cm thick. An Al strip (3×5 cm^2) with a thickness of 0.01 cm was fixed to act as the bottom electrode, over which the cleaned PTFE film was attached. For the top electrode, a narrow Al tape (0.1×4 cm^2) with a thickness of 0.01 cm was affixed to the PTFE surface. Further, for electrical measurements, positive and negative terminals were attached to the upper and lower electrodes, respectively. The image of the water sliding over the dielectric layer was extracted from a video recorded using an iPhone camera at 30 frames per second.

The electrical voltage of the LS-TENG was measured using a digital oscilloscope (M/S Tektronix, MSO44B, USA), whereas the current was measured using an electrometer (Keithley 6514, USA) coupled to a LabVIEW program. The readings were taken at the ambient temperature with a relative humidity of 30% RH. The image of water flowing through the dielectric layer was captured using a smartphone. The X-ray diffraction (XRD) pattern was traced using an XRD diffractometer (M/S Panalytical, Netherlands). The morphology and elemental mapping were done using the scanning electron microscope (SEM) (M/S Hitachi SU8230, Japan). A droplet of DI water on a PTFE layer was recorded and examined using the Ossila Contact Angle Goniometer in the UK.

3. Results and discussion

The design and components of the LS-TENG, as well as a digital image of the LS-TENG, are shown in Fig. 1a. The PTFE composite film that comprises the dielectric layer imparts superior

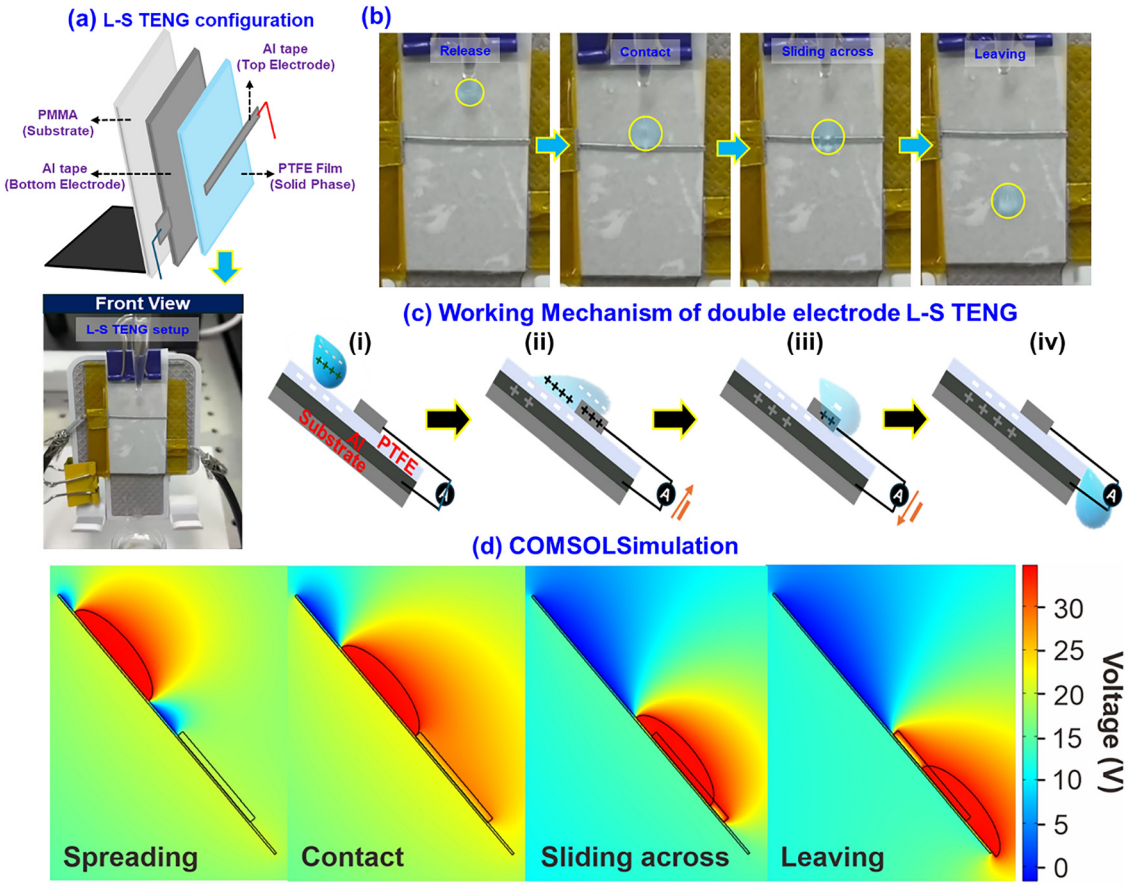

Fig. 1 (a) Illustration of the LS-TENG having a double electrode, (b) digital images of the movement pattern of the droplet over the PTFE layer, (c) working mechanism of LS-TENG, (d) surface electric potential changes when a water drop on the PTFE surface and its sliding over the Al top electrode simulated by finite element analysis.

water-repellent qualities to the surface. The upper electrode is a narrow Al tape, 0.1 × 4 cm^2. An acrylic plate serves as the supporting base, onto which an Al strip is fixed to act as the bottom electrode.

The motion of falling droplets on a dielectric surface was examined to understand how the liquid–solid contact becomes electrically charged, as shown in Fig. 1b. A droplet's contact area with the dielectric steadily increases as it spreads outward from the impact point. A constant cycle of contact, spreading, sliding, and separation is enabled by the dielectric's superhydrophobic properties, which ensure that each fresh droplet interfaces cleanly with the surface. This dynamic process is crucial for maintaining effective and stable charge generation. The LS-TENG's working principle is closely aligned with the flow of water droplets across the dielectric surface. When a droplet touches the PTFE layer, contact electrification occurs, resulting in opposite charges: positive on the droplet and negative on the film, as shown in Fig. 1c. There is no current flowing through the external circuit (i) at present. An electrical link is formed between the droplet and the surface layer when it contacts the top Al electrode as it spreads and begins to move. This interaction induces charge redistribution within the device, causing electrons from the bottom electrode to flow upward, thereby generating an output current (ii). The accumulated charges migrate back toward the bottom electrode when the droplet begins to retract and move downward, losing contact with the upper electrode (iii). The first droplet eventually separates from the surface, returning the system to its initial charge state (iv). This cycle of charge generation, transfer, and release is repeated with each new droplet that arrives, thereby generating electrical energy as droplets fall. The simulation in Fig. 1d illustrates the voltage distribution of a double-electrode LS-TENG system, in which a droplet (DI water) spreads over a PTFE surface and makes contact with the upper electrode. The PTFE surface is assigned a negative charge density of −2.60 μC m^{-2}, whereas the droplet carries a positive charge of +4.20 μC m^{-2}. As the droplet impacts and spreads across the PTFE, charge accumulation occurs at the L–S interface. When the droplet reaches the top electrode, an electron is transferred between the upper and lower electrodes through the external circuit. During the droplet's motion, the potential distribution changes rapidly. After the droplet detaches from the top electrode, its surface potential gradually rises again due to renewed contact with the PTFE. Overall, the simulation outcomes are consistent with the previously described working principle.

Fig. 2a shows the XRD pattern of the PTFE dielectric layer. The (100), (110), (200), (210), (300), (220), and (310) planes are represented by distinct and sharp diffraction peaks in the XRD pattern.[36] The strong crystallinity and organised chain organisation are indicated by the prominent (100) reflection at about 18°. The existence of several low-intensity peaks further supports the semi-crystalline structure of PTFE. Fig. 2b illustrates the hydrophobicity of PTFE, characterized by a static contact angle of 115.6°. This strong water repellency facilitates effective charge generation in the liquid–solid triboelectric interface. The hydrophobic surface ensures steady droplet rolling on PTFE, which is essential for the reliable, repeatable output performance of LS-TENG. The SEM micrograph of the PTFE surface reveals a relatively smooth and crack-free texture, as shown in Fig. 2c. After cleaning and thermal treatment, the absence of surface contaminants indicates good film integrity, which is crucial for maintaining dielectric uniformity. The spectrum confirms the elemental composition of the PTFE film as shown in Fig. 2d. The dominance of fluorine is consistent with the CF_2 structure of PTFE, which contributes to its high electronegativity and strong tendency to gain electrons during triboelectric interactions. The elemental mapping images further verify a homogeneous distribution of F, C, and O across the surface, indicating uniform material composition.

Fig. 3a shows the voltage generated by LS-TENG for two droplet impact frequencies, such as 0.3 Hz (slow drop) and 0.7 Hz (fast drop). The voltage of −37 V remains comparable, indicating that frequency affects pulse rate rather than amplitude. The linear increase in pulse density indicates stable charge transfer with increasing droplet rate, confirming frequency-dependent energy generation. Fig. S1 shows the voltage produced by various device configurations, such as double-electrode, top-electrode, and bottom-electrode LS-TENG. The output of LS-TENG varies mostly because of differences in charge transfer capacity. Charge transfer between electrodes during droplet spreading and rebounding is driven by electric double-layer formation and electrostatic induction in the LS-TENG double-electrode and top-electrode configurations, whereas in the bottom-electrode configuration, it yields lower electrical output because it relies solely on electrostatic induction. Fig. 3b shows the generated current from the LS-TENG as a droplet impacts upon the PTFE layer. The peak current of 52 nA confirms efficient charge flow through the external circuit. Fig. 3c shows the voltage of LS-TENG at various inclination angles (10°–80°) of the substrate. At small angles, insufficient droplet momentum limits the contact area, whereas at moderate angles (∼40°–50°), the droplet spreads efficiently, enhancing charge transfer and yielding the maximum voltage. The droplets roll off quickly, reducing effective contact and charge accumulation when the substrate angle exceeds 60°. Fig. 3d shows the voltage output of LS-TENG by varying droplet release heights (0.5–3 cm) from the solid PTFE layer. At a 3 cm distance between the droplet and the PTFE layer, the droplet's kinetic energy upon impact results in greater deformation and a larger contact area, thereby enabling higher charge transfer. The difference affects the amount of charge generated on the surface, the electron attraction between the contacting materials, and the droplet impact height. The liquid spreads more widely across the triboelectric layer when the droplet falls from a higher height, because it

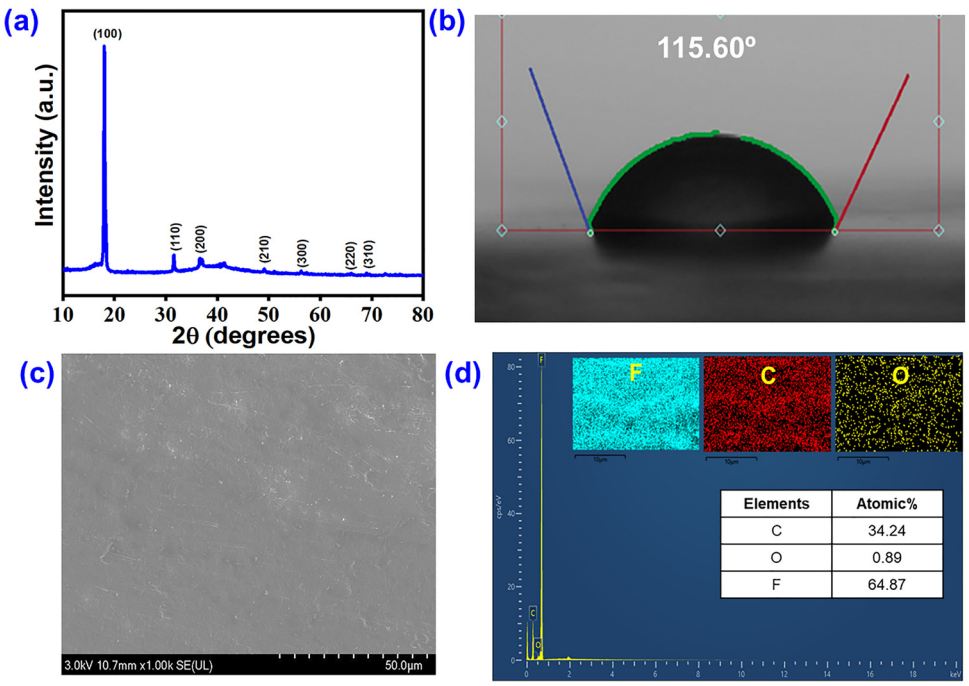

Fig. 2 (a) XRD pattern of PTFE, (b) contact angle of PTFE using DI water, (c) surface morphology of PTFE, and (d) elemental mapping and EDS spectra of PTFE layer.

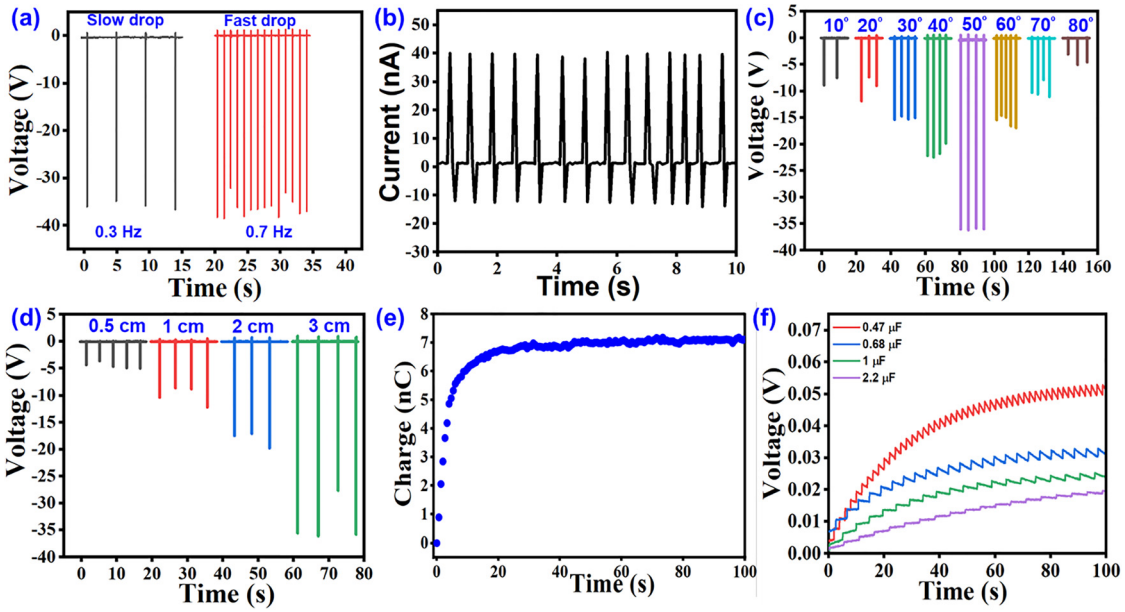

Fig. 3 (a) Voltage generated by LS-TENG at various frequencies, (b) current generated by L-TENG, (c) voltage of LS-TENG by varying the angle of substrate, (d) voltage generated by the LS-TENG by varying the distance between the pipette and solid PTFE layer, (e) charge retention of LS-TENG, and (f) charging of capacitors with varying capacitance values using LS-TENG.

hits the surface with greater impact. This expanded contact area improves charge generation. The charge output gradually increases with increasing drop height until it saturates, at which point further increases in height no longer result in a increase in charge.

Fig. 3e shows the transferred charge as a function of time during repeated droplet impacts. The charge initially increases rapidly and then saturates at 7 nC, indicating a steady-state charge balance after multiple cycles. Fig. 3f shows the charging curves of capacitors with different capacitances connected to the LS-TENG. Fig. S2a shows the circuit diagram of the LS-TENG, bridge rectifier, and the capacitor considered during the charging of capacitors using LS-TENG. The AC signal generated by the LS-TENG is converted to an DC signal using bridge rectifier circuit. Continuous charging of the capacitor demonstrates that the LS-TENG's output is stable for a longer period. The stored charge by the capacitors charged using LS-TENG was calculated by employing the formula $Q = CV$ (C = capacitance, V = voltage) as shown in Fig. S2b.

The correlation between output voltage and power at various external load resistances was systematically analysed. As illustrated in Fig. 4a, increasing the external resistance results in a gradual increase in voltage, as predicted by Ohm's law. The power output behavior, shown in Fig. 4b, indicates that the LS-TENG achieves its maximum power of approximately 8 μW at an optimal load resistance of 10^7 Ω, beyond which the power decreases due to an impedance mismatch between the device and the external circuit. Different pH solutions were prepared using commercially available standard buffer solutions with predefined pH values, which provide stable, reproducible acidity/alkalinity without further adjustment. Each buffer was used directly as the droplet solvent after pH meter calibration to ensure accuracy. Fig. 4c and d show the voltage generated by the LS-TENG at various pH levels. As the pH increases from 1 to 7, the output voltage rises sharply from approximately −0.4 V to −35 V, allowing for a clear distinction between acidic and neutral conditions. Conversely, as pH increases from 7 to 14, the output voltage decreases from −35 V to −3.9 V, indicating the sensor's ability to discriminate between acidic and basic environments. The generation of surface charge during droplet contact depends strongly on the ion concentration and type in the solution.

In acidic media (low pH), the abundance of H^+ ions enhances positive charge transfer, thereby strengthening triboelectric effects. As the pH increases toward neutral, the balance of ion concentrations reduces effective charge separation, because H^+ and OH^- are present in nearly equal amounts. In a high-pH solution, OH^- ions alter the surface potential and screening effects, thereby decreasing the net triboelectric voltage. When these OH^- ions contact the PTFE surface, they adsorb onto the surface or form part of the EDL at the solid–liquid interface. Therefore, the observed variation reflects pH-dependent interfacial ion adsorption and modulation of the electric double layer on the TENG surface, enabling the LS-TENG to be well-suited for distinguishing among acidic, neutral, and basic media. Fig. 4e presents the linear regression for acidic media (pH 1–7), with a slope of 6.4 V/pH, indicating high responsiveness in acidic conditions. In contrast, Fig. 4f presents the performance in basic media (pH 7–14), where the sensor exhibits a slightly lower voltage response slope of 4.77 V/pH. These sensitivities confirm that the sensor efficiently quantifies pH variation, with greater resolution for different conditions.

Fig. 5a illustrates the application of the LS-TENG probe in testing a sucrose solution in industrial settings. Advanced

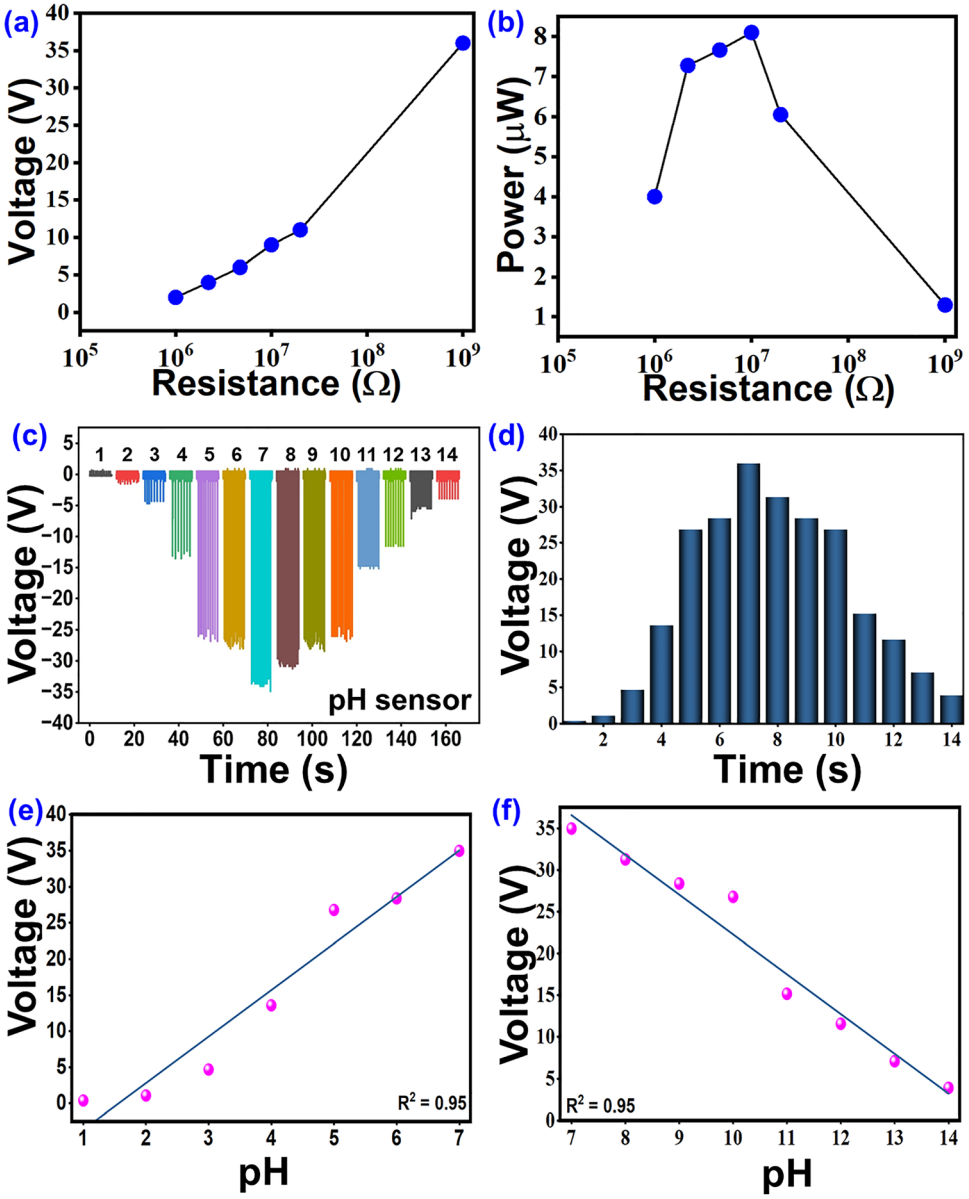

Fig. 4 (a) and (b) Voltage and power generated by LS-TENG at various load resistances, (c) and (d) voltage output of LS-TENG at various pH, (e) and (f) linear fitting of voltage generated by LS-TENG across various pH 1 to pH 14.

sensing systems are necessary for effective and real-time process control, given the rapid expansion of smart manufacturing.[37,38] High-sensitivity continuous monitoring of sucrose concentrations in fluids is possible with LS-TENG. Early detection of sugar leaks is essential because high sucrose levels in groundwater or wastewater from the sugar industry can promote the growth of microorganisms and biofilm formation.[39,40] When such contamination enters drinking systems, it can degrade water quality and pose health risks.[41] Hence, due to public health and environmental safety concerns, rapid, self-powered sucrose detection is crucial.

Sucrose droplets of different concentrations were prepared by dissolving the required weight percentage of sucrose in 50 ml of deionized water, followed by 5 minutes of bath sonication to ensure homogeneous mixing before use. Fig. 5b shows the stability of the LS-TENG output when DI water was dropped onto the PTFE surface for 120 s. Fig. 5c shows alternating ON–OFF signal responses as different sucrose solutions (DI water, 2 wt%, and 8 wt%) are introduced sequentially. The experiment demonstrates the ability of LS-TENG to identify various solution types, including deionized water, simulated sucrose, and DI–water mixtures. The alternating ON–OFF behavior of LS-TENG demonstrates suitability for real-time concentration detection without signal lag or residual charge buildup. Fig. 5d shows the voltage signals of the LS-TENG for DI water and DI water+wt% sucrose solutions bearing concentrations of 2, 4, 6, and 8 wt%.

As the sucrose concentration increases, the voltage amplitude gradually decreases. Increased sucrose concentration limits effective contact and charge separation at the interface by

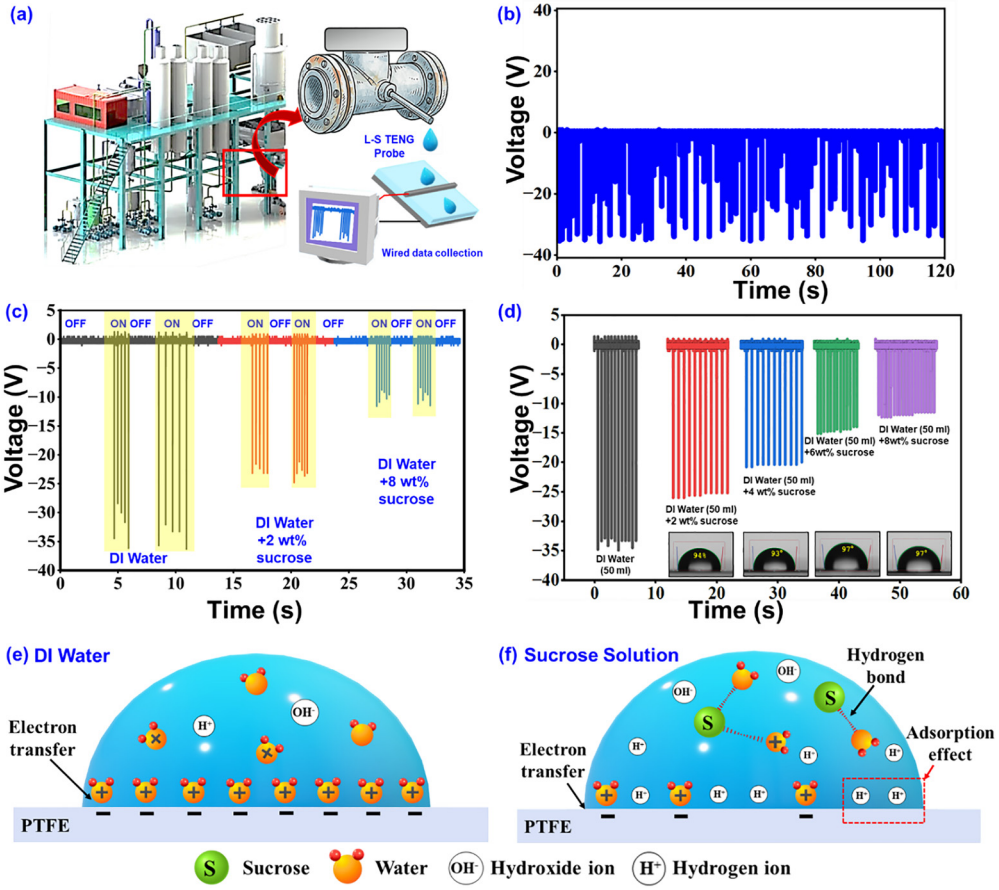

Fig. 5 (a) Schematic diagram of LS-TENG for a self-powered sucrose fluid monitoring in industries; (b) stability of the LS-TENG voltage output for 120 s, (c) electrical output voltage from different liquid impact upon LS-TENG, (d) influence of varying sucrose concentrations on the voltage of LS-TENG, (e) and (f) schematic illustration showing liquid–solid electrification between a DI water solution and a sucrose solution.

increasing the solution's viscosity and decreasing molecular mobility. Fig. S3 shows the electrical output of the LS-TENG by fixing the solid layer PTFE constant and varying the liquid, such as 50 ml of DI water+8 wt% sucrose, 50 ml of DI water mixed with 8 wt% sucrose+ 8 wt% glucose, and 50 ml of DI water mixed with 8 wt% sucrose+ 8 wt% dextrose. Larger voltage output seen for sucrose solutions indicates that the LS-TENG has a better sensing response to sucrose than to other sugars. Due to their bigger molecular structure and greater number of hydroxyl functional groups, sucrose molecules are better able to disrupt the natural hydrogen-bonding network of water. Smaller monosaccharides, such as glucose or dextrose, in contrast, modify the interfacial electrostatic environment to a lesser extent, resulting in a lower voltage output. Further, surface charges are screened by adsorbed sucrose molecules, thereby inhibiting electron transport and reducing triboelectric output. Fig. 5e and f present a schematic model of the interaction between water or a sucrose solution and the PTFE surface, elucidating how sucrose affects liquid–solid charge production. The slight presence of H^+ and OH^- ions in DI water is disregarded for simplicity. Electrons from water molecules move toward the PTFE surface when DI water contacts it (Fig. 5e), forming a negatively charged layer. Conversely, sucrose promotes hydrogen bonding, making it easier for water molecules to partially ionise, thereby creating more H^+ ions. As seen in (Fig. 5f), these protons are easily adsorbed onto the PTFE solid layer, creating a shielding layer that prevents additional electron transmission between the liquid and the solid surface, hence reducing total charge creation.

4. Conclusions

The presented LS-TENG effectively integrates energy harvesting and sucrose concentration sensing into a single platform. The dual-electrode mode LS-TENG design harnesses droplet dynamics to generate a notable electrical output, enabling real-time monitoring. Variations in sucrose levels directly affect charge transfer and voltage response, confirming the sensing capability. The results demonstrate reliable energy conversion, with a output of −37 V, 52 nA, and 8 μW of power at 10^7 Ω. Changes in hydrogen-bond interactions between water and sucrose are identified as the key sensing mechanism. The charging of capacitors was demonstrated using the electrical output produced by LS-TENG. Overall, this work establishes a

self-powered, environmentally friendly approach to intelligent sucrose monitoring in industrial systems.

Author contributions

Premkumar Sharad Bhosale: conceptualisation, writing – original draft, investigation, Sugato Hajra: writing – original draft, formal analysis, project management, Swati Panda: data curation, Kushal Ruthvik Kaja: data curation, investigation, Mohamed Belal: investigation, visualisation, Soon Moon Jeong: writing – review and editing, Hoe Joon Kim: supervision, funding acquisition, writing – review and editing.

Conflicts of interest

There are no conflicts to declare.

Data availability

The data supporting the findings of this study are available from the corresponding author upon reasonable request. All relevant data generated or analysed during this study are included in this article.

Supplementary information (SI) is available. See DOI: **https://doi.org/10.1039/d6qm00006a**.

Acknowledgements

This work was supported by the National Research Foundation of Korea (NRF) grant funded by the Ministry of Science and ICT (MSIT) (No. RS-2024-00346135, RS-2024-00406674) and the Ministry of Education (No. RS-2025-25420118). We thank Dr. Saichon Sriphan of KMUTNB, Thailand, for his help with the COMSOL simulation and Dr. Utchawadee Pharino for some measurements discussion.

References

1 N. R. Sardar, S. H. Akbari, H. G. Bhatt and R. B. Modi, Role of Sucrose Ester for Enhancing the Food Quality and Safety: A Review, *Asian J. Food Res. Nutr.*, 2024, **3**, 425–430.
2 D. Ni, Z. Chen, Y. Tian, W. Xu, W. Zhang, B. G. Kim and W. Mu, Comprehensive utilization of sucrose resources via chemical and biotechnological processes: A review, *Biotechnol. Adv.*, 2022, **60**, 107990.
3 L. R. Scarratt, L. Zhu and C. Neto, Large effective slip on lubricated surfaces measured with colloidal probe AFM, *Langmuir*, 2020, **36**, 6033–6040.
4 Y. J. Hong, M. Y. Son and Y. C. Kang, One-pot facile synthesis of double-shelled SnO2 yolk-shell-structured powders by continuous process as anode materials for Li-ion batteries, *Adv. Mater.*, 2013, **25**, 2279–2283.
5 J. Hu, M. Iwamoto and X. Chen, A Review of Contact Electrification at Diversified Interfaces and Related Applications on Triboelectric Nanogenerator, *Nano-Micro Lett.*, 2023, **16**, 7.
6 Y. Jin, C. Wu, P. Sun, M. Wang, M. Cui, C. Zhang and Z. Wang, Electrification of water: From basics to applications, *Droplet*, 2022, **1**, 92–109.
7 X. Qian, D. K. Johnson, M. E. Himmel and M. R. Nimlos, The role of hydrogen-bonding interactions in acidic sugar reaction pathways, *Carbohydr. Res.*, 2010, **345**, 1945–1951.
8 S. A. Behera, H.-G. Kim, I. R. Jang, S. Hajra, S. Panda, N. Vittayakorn, H. J. Kim and P. G. R. Achary, Triboelectric nanogenerator for self-powered traffic monitoring, *Mater. Sci. Eng., B*, 2024, **303**, 117277.
9 S. Hajra, K. R. Kaja, S. Panda, M. A. Belal, B. K. Panigrahi, P. Pakawanit and H. J. Kim, Waste based triboelectric nanogenerator for energy harvesting and self-powered sensors, *J. Cleaner Prod.*, 2025, 145591.
10 K. R. Kaja, S. Hajra, S. Panda, M. A. Belal, P. Pakawanit, N. Vittayakorn, C. Bowen, H. Khanbareh and H. J. Kim, Triboelectrification based on the waste waterproof textiles for multisource energy harvesting, *Adv. Sustainable Syst.*, 2025, **9**, 2400678.
11 K. Dong, Y.-C. Wang, J. Deng, Y. Dai, S. L. Zhang, H. Zou, B. Gu, B. Sun and Z. L. Wang, A highly stretchable and washable all-yarn-based self-charging knitting power textile composed of fiber triboelectric nanogenerators and supercapacitors, *ACS Nano*, 2017, **11**, 9490–9499.
12 R. Wen, J. Guo, A. Yu, J. Zhai and Z. L. Wang, Humidity-resistive triboelectric nanogenerator fabricated using metal organic framework composite, *Adv. Funct. Mater.*, 2019, **29**, 1807655.
13 A. Babu, S. Gupta, R. Katru, N. Madathil, A. Kulandaivel, P. Kodali, H. Divi, H. Borkar, U. K. Khanapuram and R. K. Rajaboina, Triboelectric Nanogenerators with Fe-Based Metal–Organic Frameworks, *Energy Technol.*, 2024, **12**, 2400796.
14 S. Potu, A. Kulandaivel, B. Gollapelli, U. K. Khanapuram and R. K. Rajaboina, Oxide based triboelectric nanogenerators: Recent advances and future prospects in energy harvesting, *Mater. Sci. Eng., R*, 2024, **161**, 100866.
15 K. U. Kumar, S. Hajra, G. Mohana Rani, S. Panda, R. Umapathi, S. Venkateswarlu, H. J. Kim, Y. K. Mishra and R. R. Kumar, Revolutionizing waste-to-energy: harnessing the power of triboelectric nanogenerators, *Adv. Compos. Hybrid Mater.*, 2024, **7**, 91.
16 X. Wei, Z. Zhao, C. Zhang, W. Yuan, Z. Wu, J. Wang and Z. L. Wang, All-weather droplet-based triboelectric nanogenerator for wave energy harvesting, *ACS Nano*, 2021, **15**, 13200–13208.
17 S. A. Behera, S. Hajra, S. Panda, A. K. Sahu, P. Alagarsamy, Y. K. Mishra, H. J. Kim and P. G. R. Achary, Synergistic energy harvesting and humidity sensing with single electrode triboelectric nanogenerator, *Ceram. Int.*, 2024, **50**, 37193–37200.
18 Y. Xu, Z. Sun, Z. Bai, H. Shen, R. Wen, F. Wang, G. Xu and C. Lee, Bionic e-skin with precise multi-directional droplet

sliding sensing for enhanced robotic perception, *Nat. Commun.*, 2024, **15**, 6022.
19 Y. Zi, H. Guo, Z. Wen, M.-H. Yeh, C. Hu and Z. L. Wang, Harvesting low-frequency (< 5 Hz) irregular mechanical energy: a possible killer application of triboelectric nanogenerator, *ACS Nano*, 2016, **10**, 4797–4805.
20 G. Cheng, T. Zhang, X. Fu, J. Hua, W. Dai, J. Cao, W. Sun and J. Ding, A comprehensive review of advancements and challenges from solid–solid to liquid–solid triboelectric nanogenerators, *Adv. Mater. Technol.*, 2024, **9**, 2301588.
21 K. R. Kaja, S. Hajra, S. Panda, M. A. Belal, U. Pharino, H. Khanbareh, N. Vittayakorn, V. Vivekananthan, C. Bowen and H. J. Kim, Exploring liquid-solid interface based triboelectrification, structures, and applications, *Nano Energy*, 2024, **131**, 110319.
22 Z. Yuan and L. Guo, Recent advances in solid–liquid triboelectric nanogenerator technologies, affecting factors, and applications, *Sci. Rep.*, 2024, **14**, 10456.
23 L. Jiang, X. Liu, J. Lv, G. Li, P. Yang, Y. Ma, H. Zou and Z. L. Wang, Fluid-based triboelectric nanogenerators: unveiling the prolific landscape of renewable energy harvesting and beyond, *Energy Environ. Sci.*, 2024, **17**, 3700–3738.
24 A. Kulandaivel, S. Potu, A. Babu, N. Madathil, M. Velpula, R. K. Rajaboina and U. K. Khanapuram, Advances in Ferrofluid-Based Triboelectric Nanogenerators: Design, Performance, and Prospects for Energy Harvesting Applications, *Nano Energy*, 2023, 109110.
25 A. Kulandaivel, S. Potu, R. K. Rajaboina and U. K. Khanapuram, Exploring Wettability: A Key to Optimizing Liquid–Solid Triboelectric Nanogenerators, *ACS Appl. Mater. Interfaces*, 2024, **16**, 58029–58059.
26 N. Zhang, H. Gu, K. Lu, S. Ye, W. Xu, H. Zheng, Y. Song, C. Liu, J. Jiao and Z. Wang, A universal single electrode droplet-based electricity generator (SE-DEG) for water kinetic energy harvesting, *Nano Energy*, 2021, **82**, 105735.
27 D. Wang, Q. Sun, M. J. Hokkanen, C. Zhang, F.-Y. Lin, Q. Liu, S.-P. Zhu, T. Zhou, Q. Chang and B. He, Design of robust superhydrophobic surfaces, *Nature*, 2020, **582**, 55–59.
28 X. Li, L. Zhang, Y. Feng, X. Zhang, D. Wang and F. Zhou, Solid–liquid triboelectrification control and antistatic materials design based on interface wettability control, *Adv. Funct. Mater.*, 2019, **29**, 1903587.
29 S. S. Bano, Q. Zeng and M. Arslan, Enhancing Durability and Performance of Solid–Liquid Triboelectric Nanogenerators through Advanced Corrosion-Resistant Coatings, *ChemNanoMat*, 2025, **11**, e202500054.
30 Y. Dong, N. Wang, D. Yang, J. Wang, W. Lu and D. Wang, Robust solid-liquid triboelectric nanogenerators: mechanisms, strategies and applications, *Adv. Funct. Mater.*, 2023, **33**, 2300764.
31 Y. Zhang, T. Pähtz, Y. Liu, X. Wang, R. Zhang, Y. Shen, R. Ji and B. Cai, Electric field and humidity trigger contact electrification, *Phys. Rev. X*, 2015, **5**, 011002.
32 X. Li, X. Ning, L. Li, X. Wang, B. Li, J. Li, J. Yin and W. Guo, Performance and power management of droplets-based electricity generators, *Nano Energy*, 2022, **92**, 106705.
33 B. Luo, X. Wang, T. Liu, C. Cai, Y. Liu, S. Zhang, M. Chi, C. Gao, J. Wang and Z. Liu, Liquid–solid triboelectric probes for bubbles status monitoring, *Adv. Funct. Mater.*, 2024, **34**, 2315725.
34 K. Manojkumar, M. Muthuramalingam, D. Sateesh, S. Hajra, S. Panda, H. J. Kim, A. Sundaramoorthy and V. Vivekananthan, Advances in triboelectric energy harvesting at liquid–liquid interfaces, *ACS Appl. Energy Mater.*, 2025, **8**, 659–682.
35 Y. Dong, S. Xu, C. Zhang, L. Zhang, D. Wang, Y. Xie, N. Luo, Y. Feng, N. Wang and M. Feng, Gas-liquid two-phase flow-based triboelectric nanogenerator with ultrahigh output power, *Sci. Adv.*, 2022, **81**, eadd0464.
36 J. Si, R. Ma, Y. Wu, Y. Dong and K. Yao, Microstructure and magnetic properties of novel powder cores composed of iron-based amorphous alloy and PTFE, *J. Mater. Sci.*, 2022, **57**, 8154–8166.
37 S. Sahoo and C.-Y. Lo, Smart manufacturing powered by recent technological advancements: A review, *J. Manuf. Syst.*, 2022, **64**, 236–250.
38 C. P. Vo, M. Shahriar, C. D. Le and K. K. Ahn, Mechanically active transducing element based on solid–liquid triboelectric nanogenerator for self-powered sensing, *Int. J. Precision Eng. Manuf.-Green Technol.*, 2019, **6**, 741–749.
39 J.-N. Cai, H.-M. Choi and J.-G. Jeon, Relationship between sucrose concentration and bacteria proportion in a multi-species biofilm, *J. Oral Microbiol.*, 2021, **13**, 1910443.
40 A. Zore, F. Rojko, N. M. Mlinarić, J. Veber, A. Učakar, R. Štukelj, A. Pondelak, A. Sever Škapin and K. Bohinc, Effect of Sucrose Concentration on Streptococcus mutans Adhesion to Dental Material Surfaces, *Coatings*, 2024, **14**, 165.
41 B. I. Nwadike, O. I. Falodun and A. A. Ogunjobi, Bacterial and viral contaminants in drinking water: Why do they really matter to us, in *Environmental Pollution and Public Health*, Elsevier, 2024, pp. 3–28.